S1 Introduction

This supporting information provides additional text and figures to support the main manuscript.

S2 AF curves for all soot samples and sizes 1 µm OPC chanel

This section contains the complete activation curves for the different soot types. Data shown corresponds to the 1 µm channel of the OPC, i.e. detecting particles that are equal/larger to the (optical) size selected for the OPC channel. Size selection was achieved using a DMA with aerosol to sheath flow ratios of 1:10 for $100-300$ nm soot particles and 1:7 for 400 nm particles, respectively, as noted in SI Table S1 (F_{DMA}). We observe no ice nucleation in the MPC regime, but cannot completely exclude the possibility of ice crystals forming in parallel to cloud droplets at/above WDS evaluating the ice nucleation experiments at this OPC channel. However, some soot types show ice formation ability in the cirrus cloud regime as discussed in the main text Sect. 3.2.

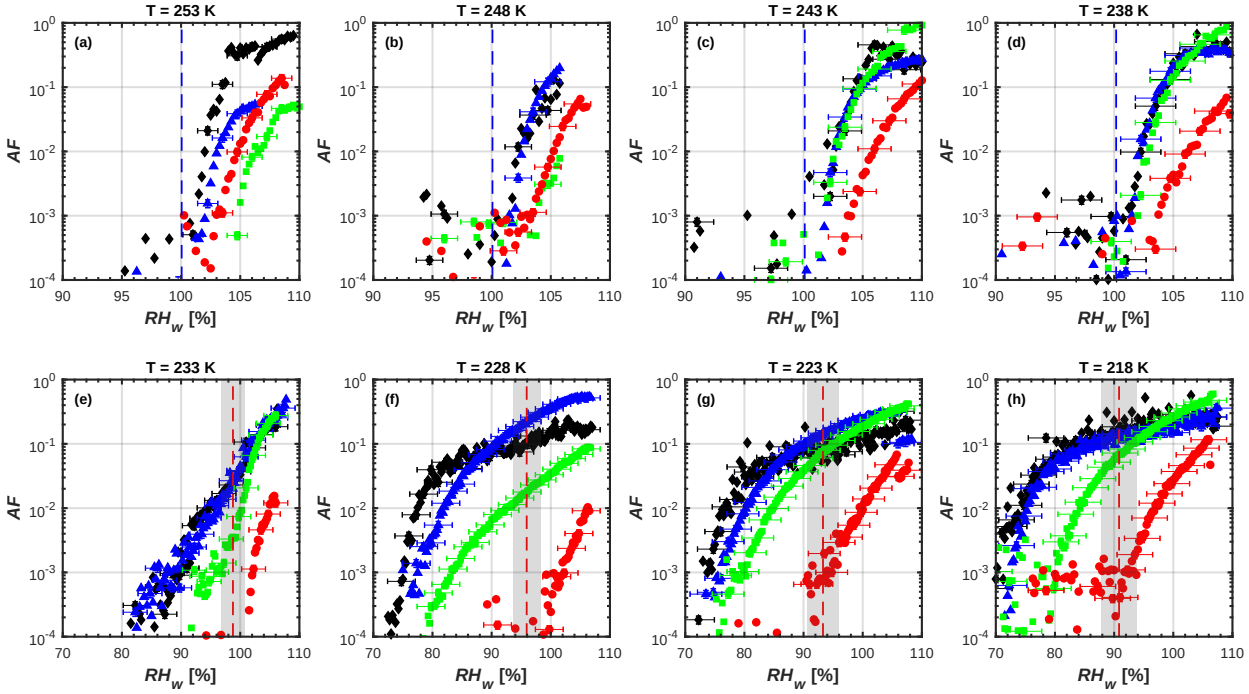

Figure S1. Relative humidity scans at constant temperature of FW200 soot particles, showing AF as a function of RH_{w} for different temperatures in the MPC regime (top row) and cirrus cloud regime (bottom row) for electrical mobility diameters of 100 nm (red circles), 200 nm (green squares), 300 nm (blue triangles) and 400 nm (black diamonds). Symbol types match those used in the main text. In each subpanel the red dashed line indicates homogeneous freezing conditions according to Koop et al. (2000) for a water-activity criterion of $\Delta a_{\mathrm{w}} = 0.305$. Similarly, vertical, blue dashed lines indicate WDS conditions for an initial droplet diameter of 100 nm, a residence time within HINC of $\tau \approx 16$ s and assuming pure diffusional growth based on Rogers and Yau (1989). Uncertainties in RH_{w} are given as the mean spread in humidity across the aerosol lamina as detailed in Appendix E1. Error in AF is ± 14 %. All curves represent mean values over all humidity scans performed at a given temperature and for a given size. For clarity error bars are only given for each 5^{th} data point.

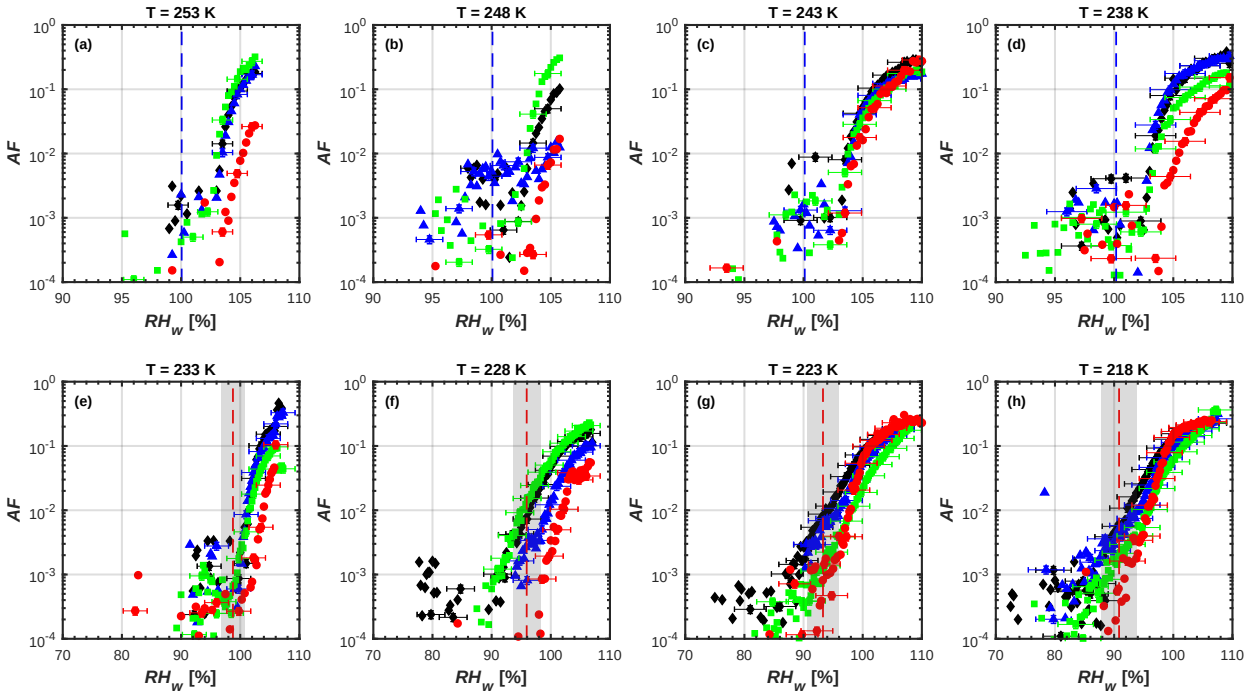

Figure S2. Relative humidity scans at constant temperature of LB_OEC soot particles. Symbols and reference lines as in Fig. S1.

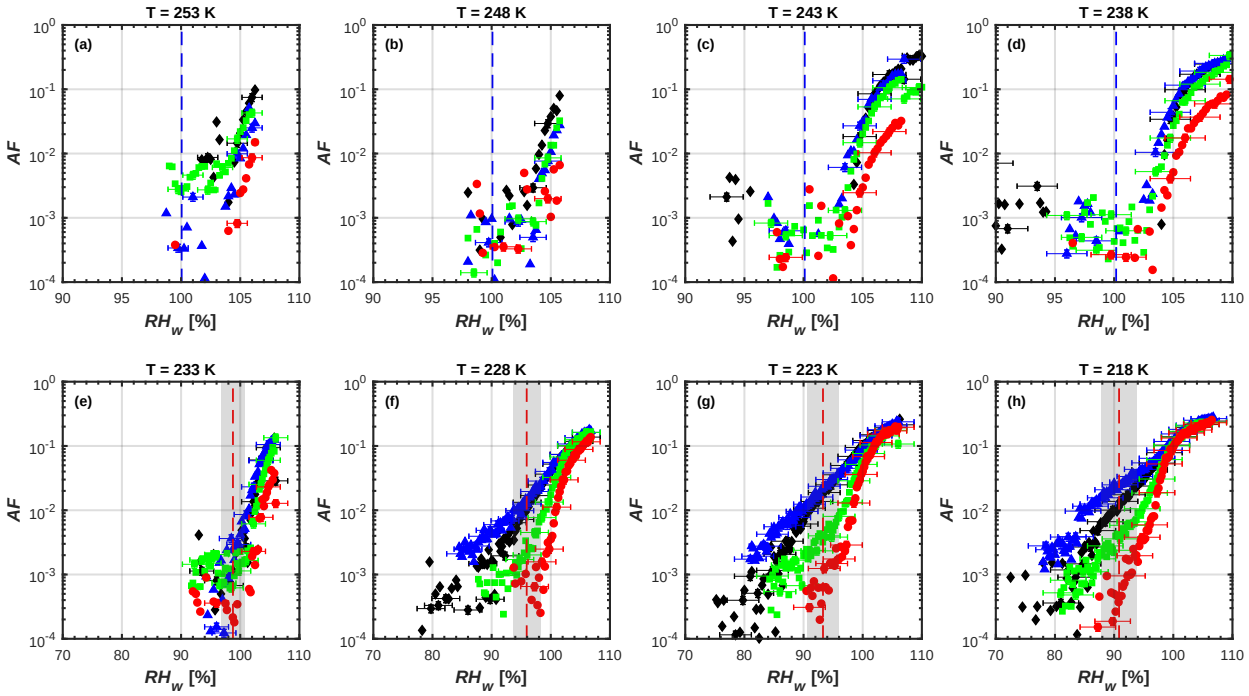

Figure S3. Relative humidity scans at constant temperature of LB_RC soot particles. Symbols and reference lines as in Fig. S1.

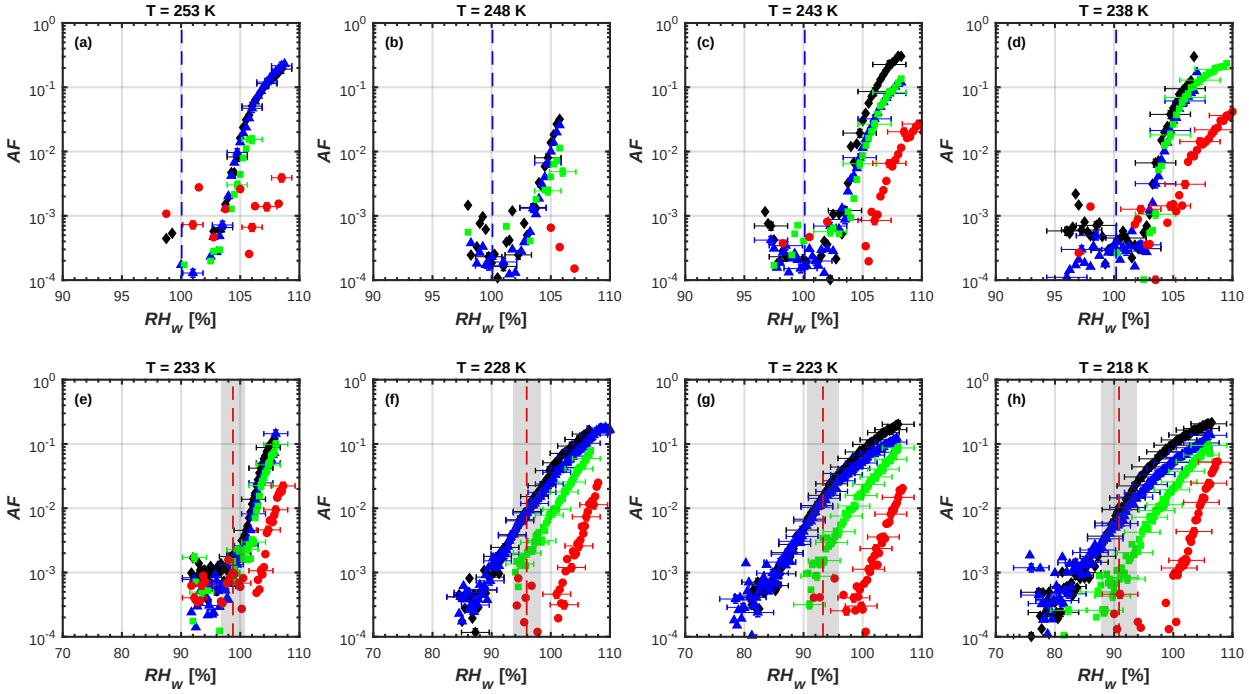

Figure S4. Relative humidity scans at constant temperature of FS soot particles. Symbols and reference lines as in Fig. S1.

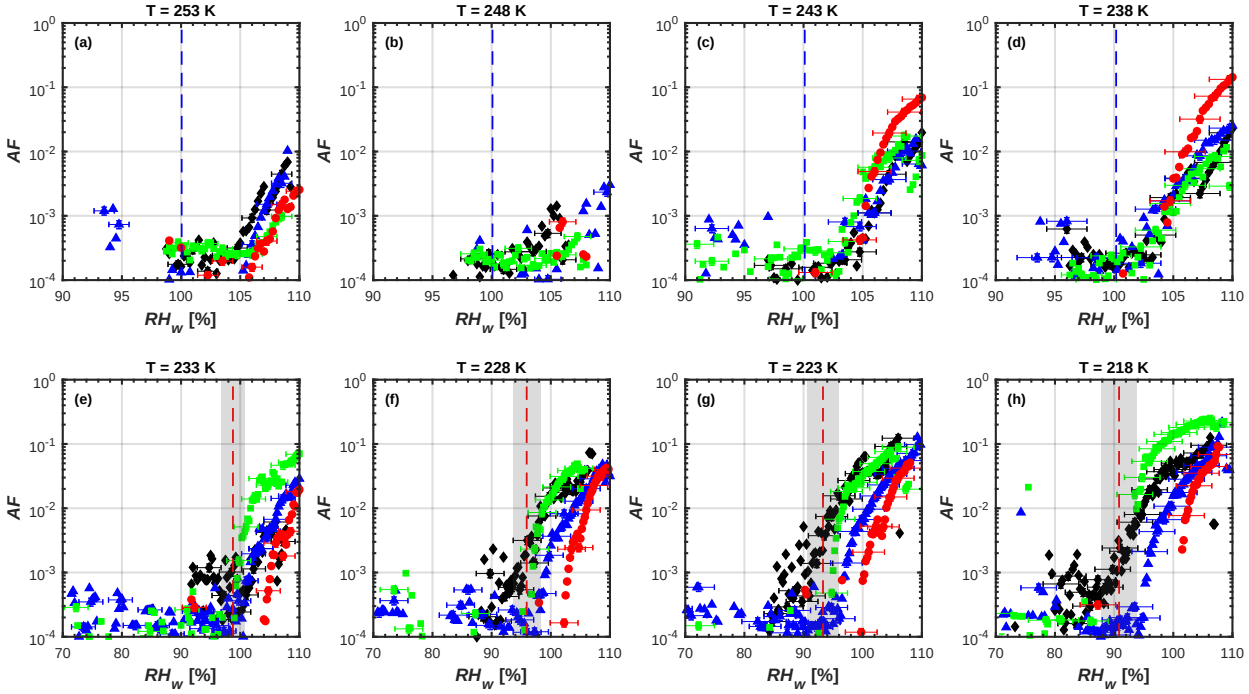

Figure S5. Relative humidity scans at constant temperature of mCAST black soot particles. Symbols and reference lines as in Fig. S1.

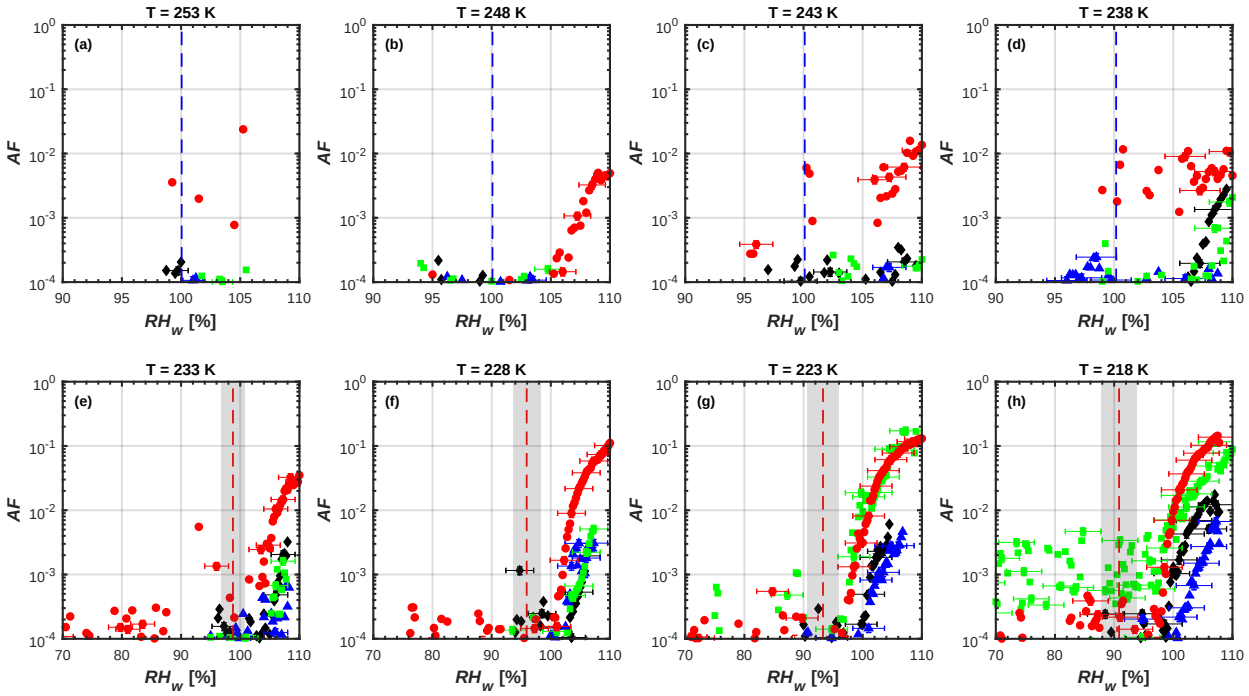

Figure S6. Relative humidity scans at constant temperature of mCAST brown soot particles. Symbols and reference lines as in Fig. S1.

S3 AF curves for all soot samples and sizes 5 µm OPC chanel

This section contains the complete activation curves for the different soot types. Data shown corresponds to the 5 µm channel of the OPC, i.e. detecting particles that are equal/larger to the (optical) size selected for the OPC channel. Size selection was achieved using a DMA with aerosol to sheath flow ratios of 1:10 for $100-300$ nm soot particles and 1:7 for 400 nm particles, respectively, as noted in SI Table S1 (F_{DMA}). We observe no ice nucleation in the MPC regime. However, some soot types show ice formation ability in the cirrus cloud regime as discussed in the main text Sect. 3.2.

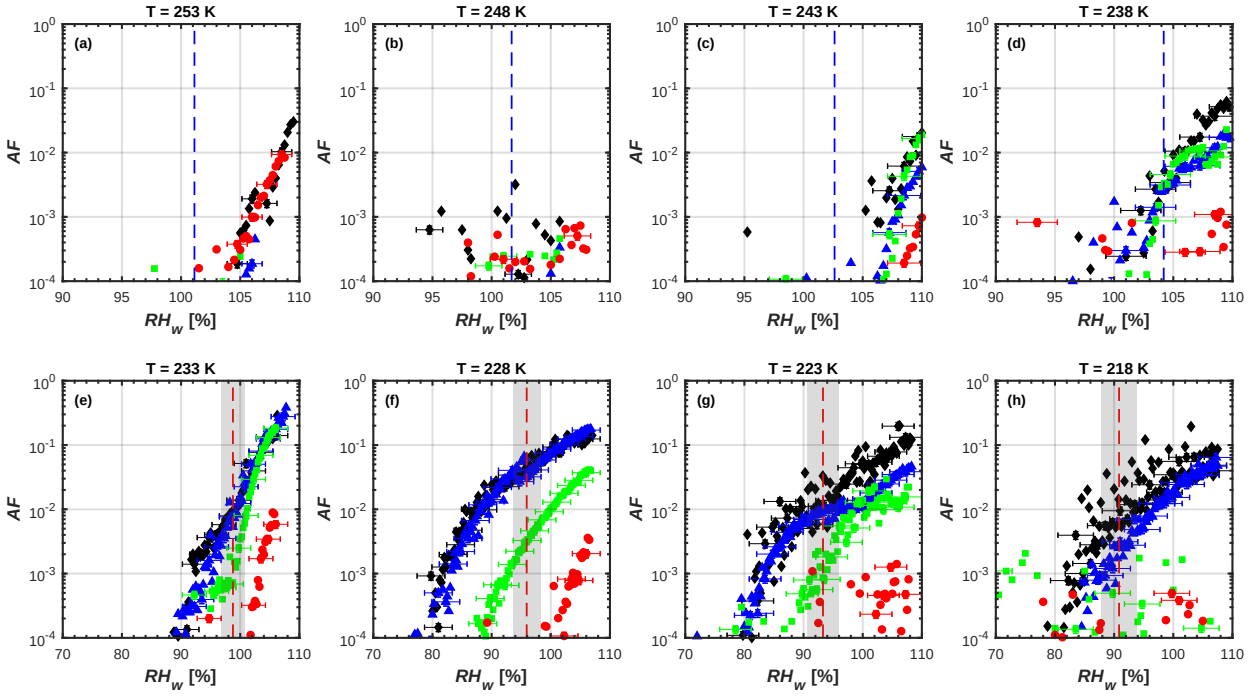

Figure S7. Relative humidity scans at constant temperature of FW200 soot particles, showing AF as a function of RH_{w} for different temperatures in the MPC regime (top row) and cirrus cloud regime (bottom row) for electrical mobility diameters of 100 nm (red circles), 200 nm (green squares), 300 nm (blue triangles) and 400 nm (black diamonds). Symbol types match those used in the main text. In each subpanel the red dashed line indicates homogeneous freezing conditions according to Koop et al. (2000) for a water-activity criterion of $\Delta a_{\mathrm{w}} = 0.305$. Similarly, vertical, blue dashed lines indicate WDS conditions for an initial droplet diameter of 100 nm, a residence time within HINC of $\tau \approx 16$ s and assuming pure diffusional growth based on Rogers and Yau (1989). Uncertainties in RH_{w} are given as the mean spread in humidity across the aerosol lamina as detailed in Appendix E1. Error in AF is ± 14 %. All curves represent mean values over all humidity scans performed at a given temperature and for a given size. For clarity error bars are only given for each 5^{th} data point.

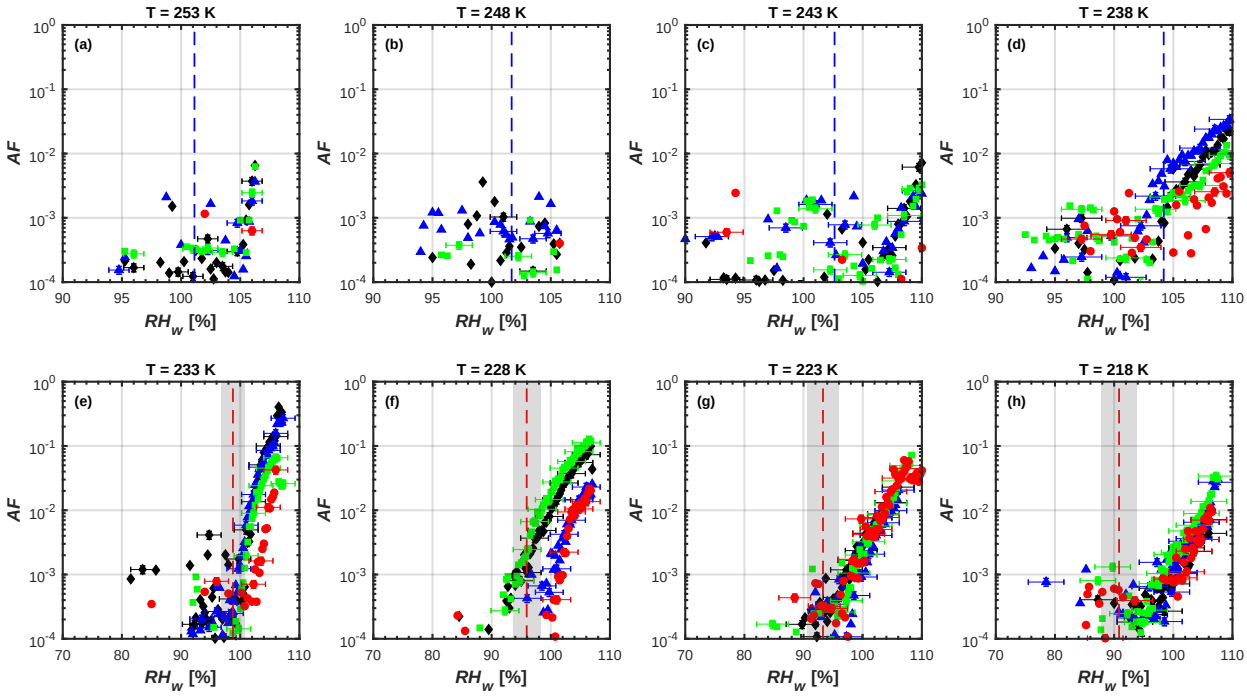

Figure S8. Relative humidity scans at constant temperature of LB_OEC soot particles. Symbols and reference lines as in Fig. S7.

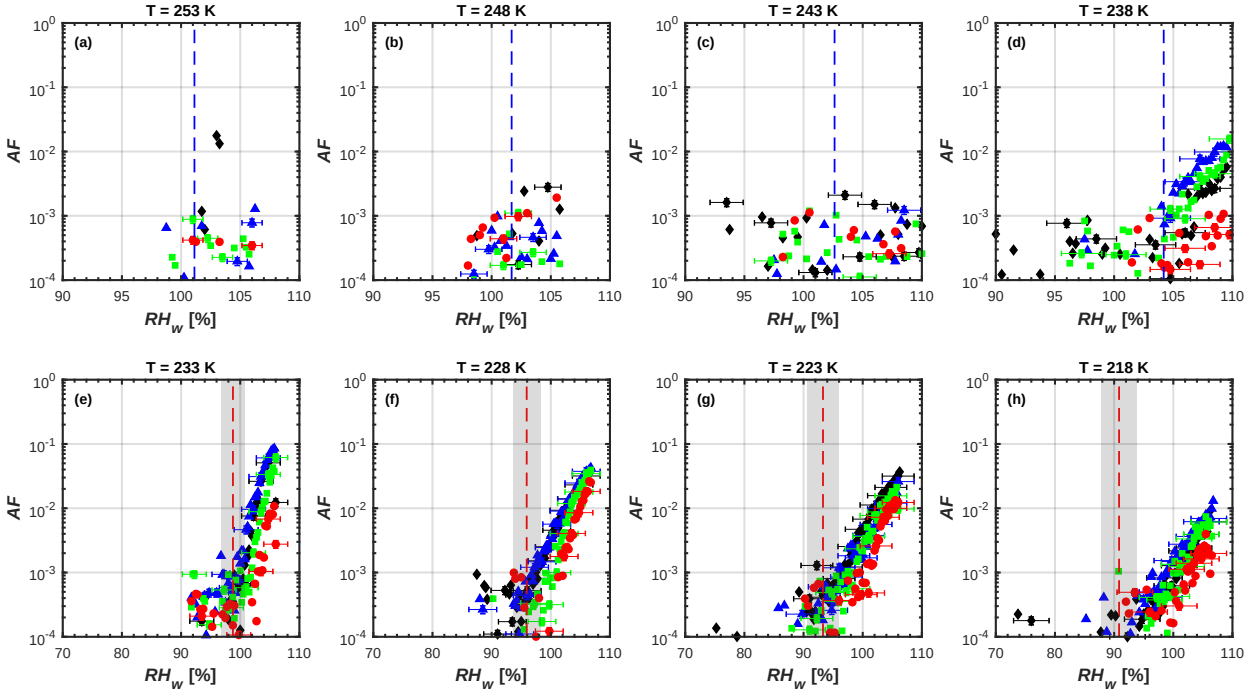

Figure S9. Relative humidity scans at constant temperature of LB_RC soot particles. Symbols and reference lines as in Fig. S7.

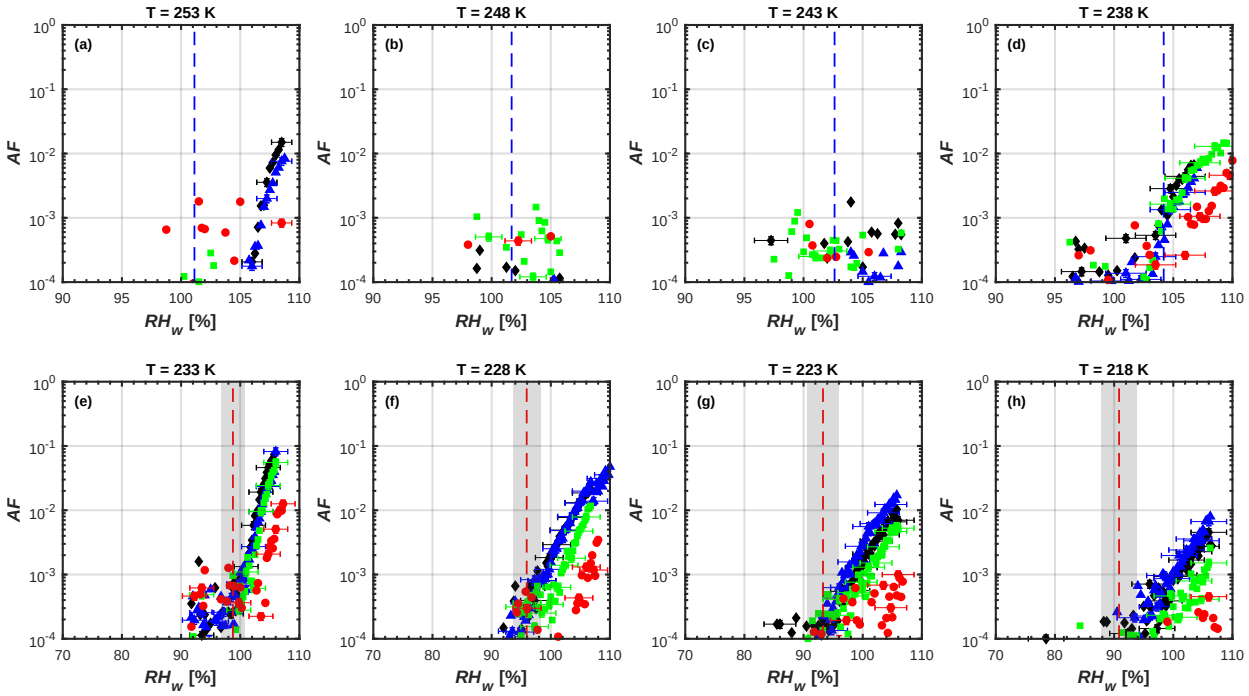

Figure S10. Relative humidity scans at constant temperature of FS soot particles. Symbols and reference lines as in Fig. S7.

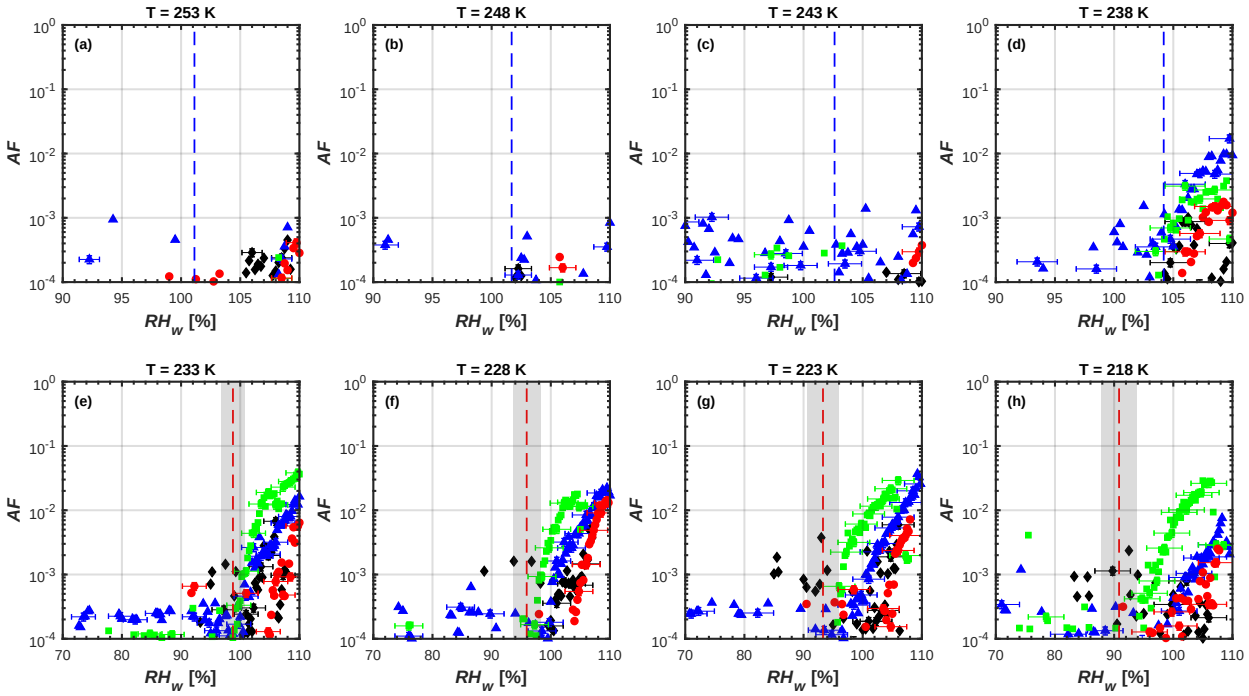

Figure S11. Relative humidity scans at constant temperature of mCAST black soot particles. Symbols and reference lines as in Fig. S7.

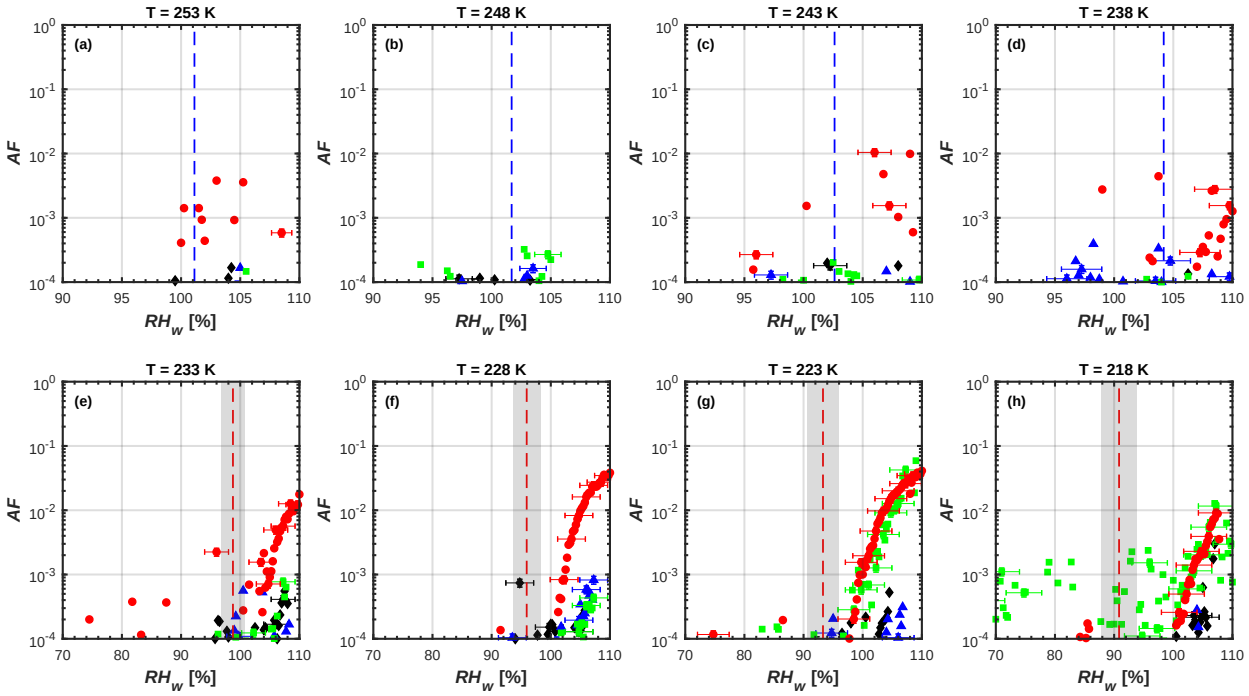

Figure S12. Relative humidity scans at constant temperature of mCAST brown soot particles. Symbols and reference lines as in Fig. S7.

S4 TGA results

Figure S13 shows the mass loss rates, corresponding to our TGA experiments to support the interpretation of the mass loss reported in Sect. 3.4 of the main text.

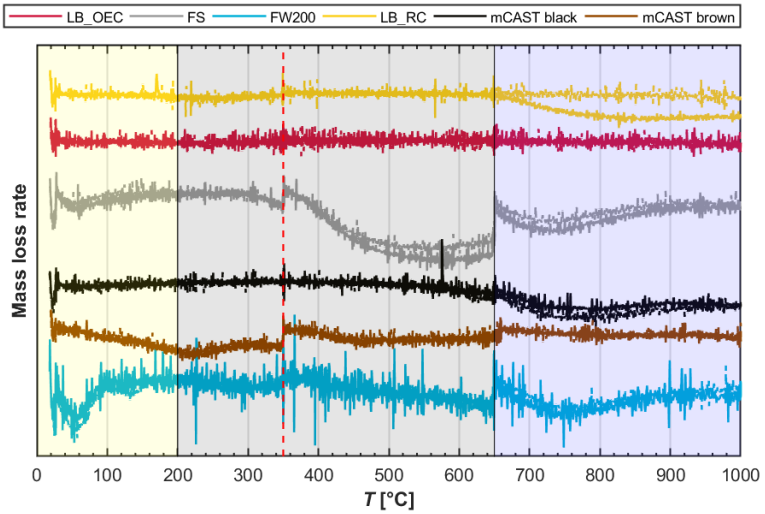

Figure S13. Mass change rate ($\%w/w/^{\circ}C$) as a function of sample temperature. Curves are shown with an offset to allow for better comparison. Solid and dashed lines indicate individual TGA runs. Shading corresponds to different ranges of heat sensitivity, namely adsorbed water and highly heat sensitive material (yellow), medium heat sensitive material/OM (gray) and low heat sensitive material (blue). Pyrolysis is expected to contribute to mass loss at temperatures above those indicated by the vertical red dashed line.

S5 DVS results

Figure S14 exemplarily shows the relative mass change (blue line) and the logarithm of the mass change rate (orange line) for a drying cycle of the FW200 soot, performed prior to DVS measurements. Drying was achieved through continuous flushing with N_2 at atmospheric pressure and a constant temperature of $T = 298$ K, at a relative water vapor pressure (p/p_0) of zero. From Figure S14 it becomes clear that the strongest mass loss occurs within the first few minutes (blue line), but that more than hundred minutes are required to completely dry the sample, as indicated by the noisy part of the orange line starting at times around $t = 200$ min, where the sample mass change rate approaches the detection limit of the instrument.

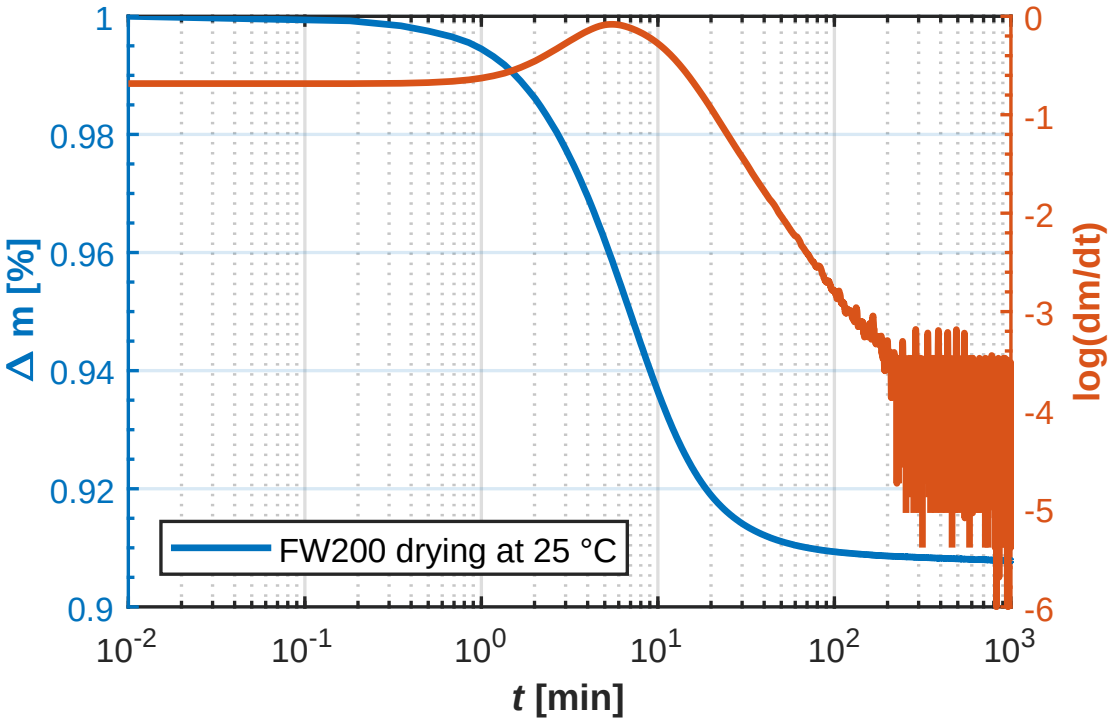

Figure S14. Relative mass loss (blue line, left hand ordinate) and logarithm of the mass loss rate (orange line, right hand ordinate) as a function of time, for an exemplary drying cycle of FW200 prior to DVS measurements.

S6 Quality of soot particle size selection

DMAs select particles based on electrical mobility size, which is identical to the physical diameter only for perfectly spherical particles, a poor assumption for soot particles (DeCarlo et al., 2004). We tested the size selection of the soot aerosols, by measuring the number size distribution of the size selected soot aerosol with an SMPS. Therefore we first size selected the soot aerosol in a DMA (Model: classifier 3080, column 3081, TSI Inc.), as was done for all our ice nucleation measurements, and subsequently measured the size distribution using another SMPS (Model: classifier 3082, column 3081, CPC 3772, TSI Inc.) downstream of the DMA. The aerosol to sheath flows used in the respective instruments are reported in Table S1. Exemplary size distributions are shown in Fig. S15 for FS soot, where the number size distribution is given in terms of number percentage corresponding to a given mobility size for ease of comparison. The sharpness of the size selection by the DMA depends on the transfer function, causing the resulting particles to spread in size around the selected midpoint diameter. The transfer func-

tion is preliminarily determined by the aerosol to sheath flow ratios within the DMA and SMPS reported in Table S1. Some heterogeneity in particle size results from different orientations of the fractal soot aggregates within the (electric field of the) DMA, as well as the presence of larger, multiply-charged particles. Finally, reliable size distribution measurements of fractal soot aggregates have been shown to be dependent on the primary particle size (Lall and Friedlander, 2006; Dastanpour et al., 2016). Here, we note in general a better size selection for smaller particles, consistent with Park et al. (2004), who reported smaller diesel soot particles to be more compact, likely resulting in a better size selection for smaller aggregates.

Table S1. Electrical mobility diameter, d_m, used for size selection within DMA along with aerosol to sheath flow ratio in DMA (F_{DMA}) and SMPS (F_{SMPS}) used for size selection and size distribution measurements, respectively. Flows are given in volumetric liters per minute. DMA used for size selection: classifier 3080, column 3081 (polonium neutralizer). SMPS used for size distribution measurement: classifier 3082, column 3081 (X-ray neutralizer), CPC 3772.

d_m [nm]	F_{DMA}	F_{SMPS}
100	1/10	1/6
200	1/10	1/6
300	1/10	1/4
400	1/7	1/4

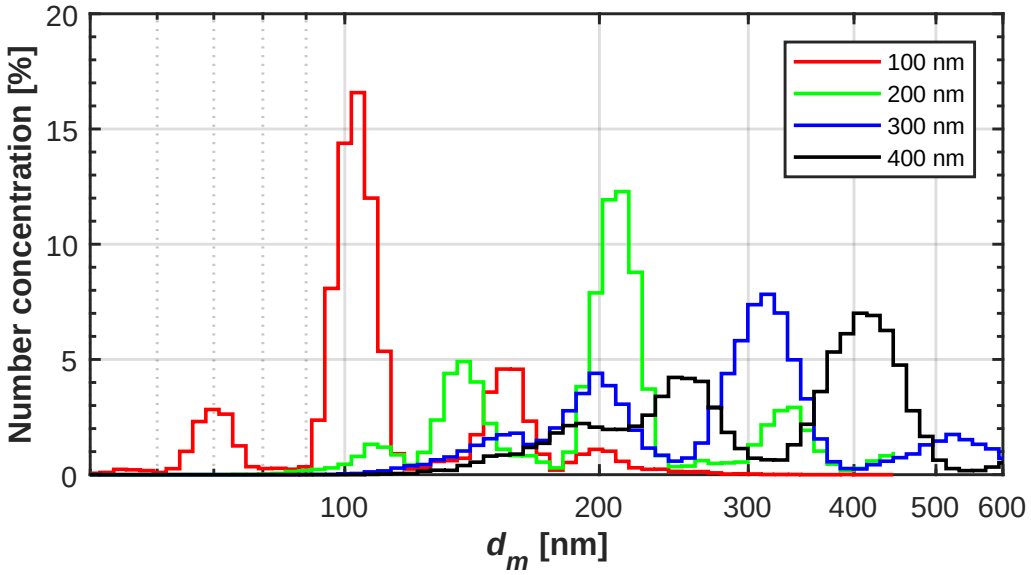

Figure S15. Number size distribution in terms of particle percentage corresponding to a given electrical mobility diameter, d_m, for size selected aerosols of FS soot, using the settings given in Table S1.

S7 Chamber validation

Chamber performance has been tested and documented in Lacher et al. (2017). Figure S16 exemplarily shows AF curves for 200 nm NH_4NO_3 obtained from our two CFDCs HINCST and HINCNE run in parallel, to verify chamber performance and intercomparability of the two ice chambers within instrumental uncertainty.

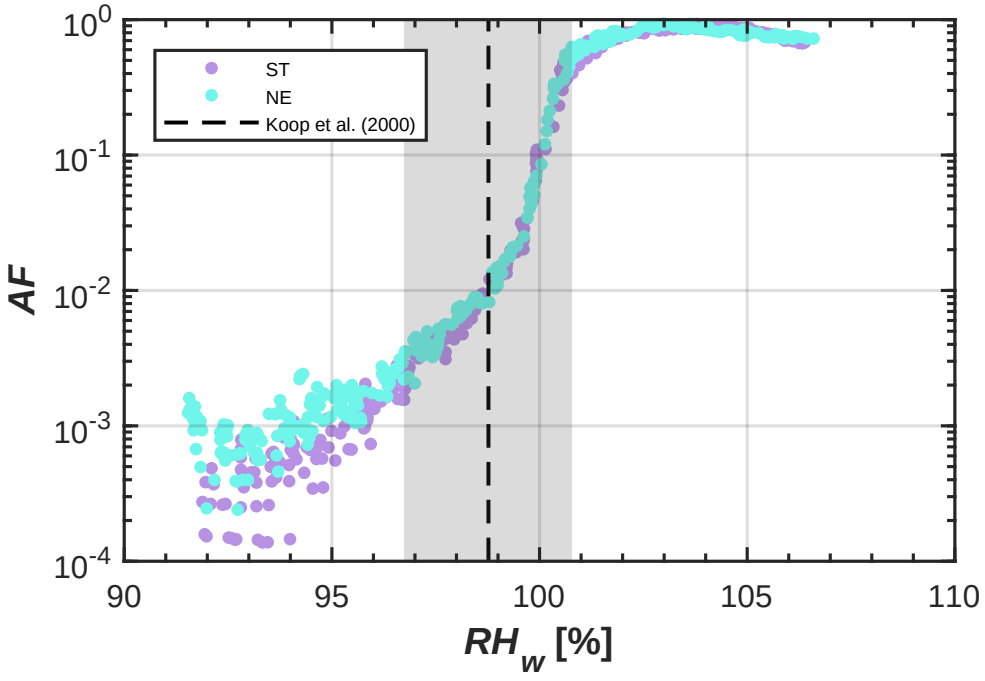

Figure S16. Exemplary RH_w scans of HINCST and HINCNE at $T = 233$ K using 200 nm NH_4NO_3 and a residence time of $\tau \approx 10.4$ s. The vertical black dashed line represents expected homogeneous freezing conditions according to Koop et al. (2000) and the gray shading indicates variation in relative humidity across the aerosol lamina. Data corresponds to the 1 µm OPC channel.

S8 TEM analysis

We have used TEM to qualitatively determine primary particle diameters and overall aggregate morphology. In Fig. S17 we show the primary particle size distribution for the different soot types, as derived from analysis of TEM images having a minimum magnification of x20k. We note that the FW200, mCAST brown and black show a narrow primary particle size distribution, whereas the lamp blacks and the FS have a broader size distribution, consistent with our TEM images discussed in the main text and shown below. In order to support the exemplary TEM images shown in the main text, Fig. S18 shows an extended selection of TEM images of the different soot types. From the images taken at the lowest magnification (left column) it becomes clear, that the size-selected soot aggregates still show a considerable heterogeneity in terms of overall aggregate size and structure, supporting our size selection reported in Fig. S15. However, quantification of these effects are beyond the scope of the present study. Finally, the presented images give examples of the studied aerosol types, but do not necessarily represent particles that were tested for ice nucleation, as the particles could undergo changes when impacting on the TEM grid. This becomes clear from Fig. S18a1, where the smaller particles are believed to result from splattering of the larger aggregate when impacting on the TEM grid.

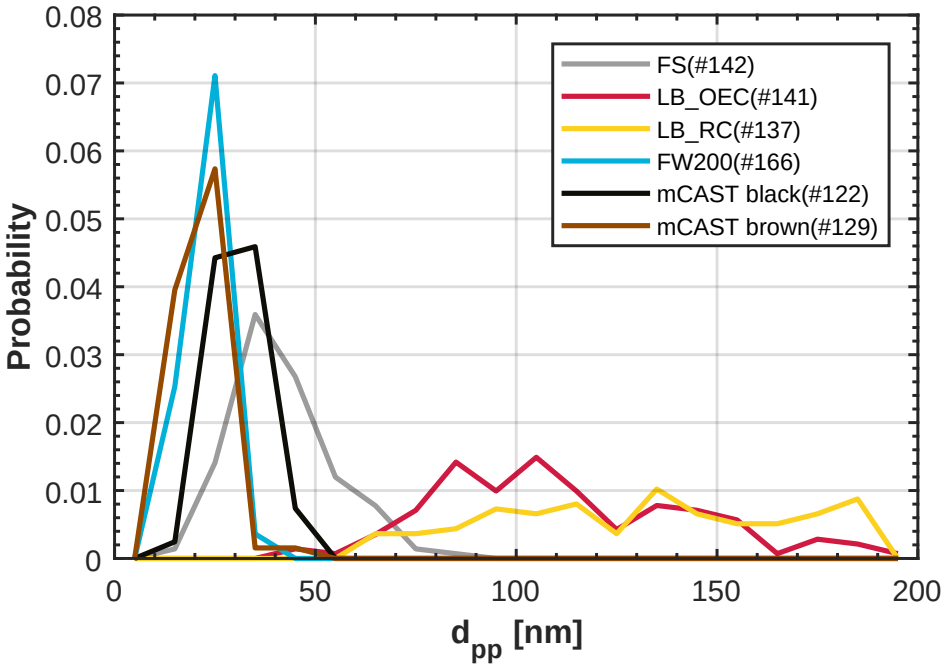

Figure S17. Distribution of primary particle sizes for the different soot types, derived from evaluation of TEM images. The number in bracktes indicates the number of primary particles sized for the corresponding soot type.

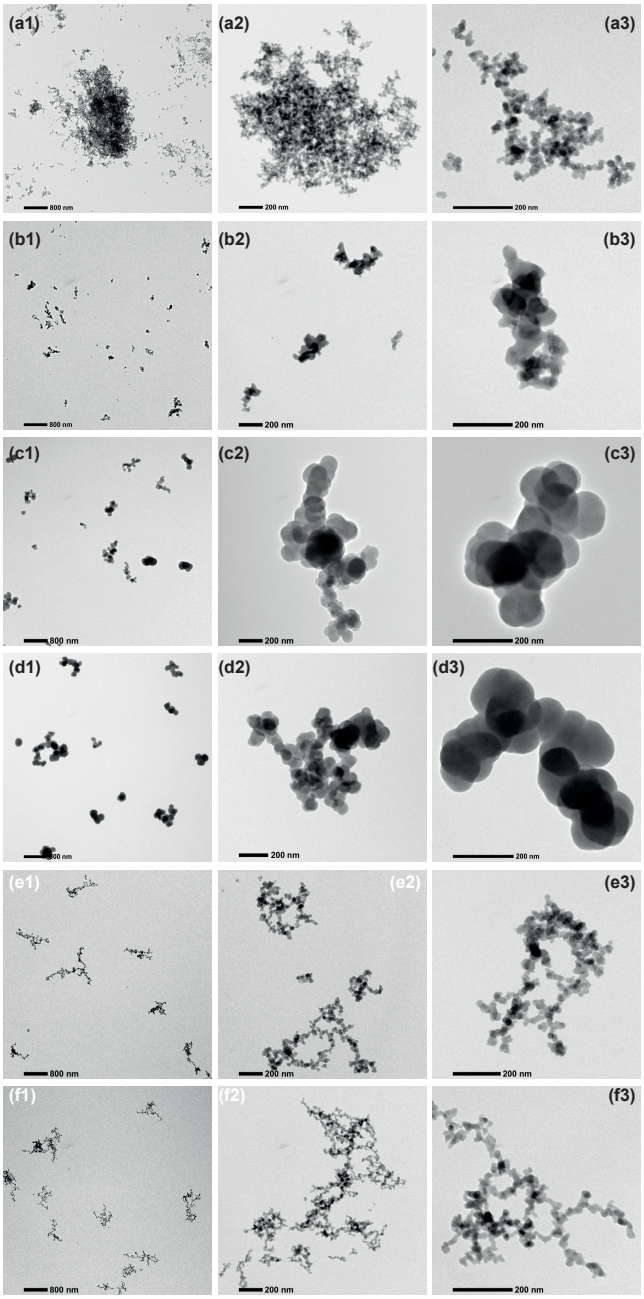

Figure S18. Exemplary TEM images of typical 400 nm mobility diameter selected soot aggregates of (a) FW200, (b) FS, (c) LB_OEC, (d) LB_RC, (e) mCAST black and (f) mCAST brown. Images of the different coloumns were taken at different magnification, but with the same microscope.

References

Dastanpour, R., Boone, J. M., and Rogak, S. N.: Automated primary particle sizing of nanoparticle aggregates by TEM image analysis, Powder Technology, 295, 218–224, 2016.

DeCarlo, P. F., Slowik, J. G., Worsnop, D. R., Davidovits, P., and Jimenez, J. L.: Particle morphology and density characterization by combined mobility and aerodynamic diameter measurements. Part 1: Theory, Aerosol Science and Technology, 38, 1185–1205, 2004.

Koop, T., Luo, B. P., Tsias, A., and Peter, T.: Water activity as the determinant for homogeneous ice nucleation in aqueous solutions, Nature, 406, 611–614, 2000.

Lacher, L., Lohmann, U., Boose, Y., Zipori, A., Herrmann, E., Bukowiecki, N., Steinbacher, M., and Kanji, Z. A.: The Horizontal Ice Nucleation Chamber (HINC): INP measurements at conditions relevant for mixed-phase clouds at the High Altitude Research Station Jungfraujoch, Atmospheric Chemistry and Physics, 17, 15 199–15 224, 2017.

Lall, A. A. and Friedlander, S. K.: On-line measurement of ultrafine aggregate surface area and volume distributions by electrical mobility analysis: I. Theoretical analysis, Journal of Aerosol Science, 37, 260–271, 2006.

Park, K., Kittelson, D. B., and McMurry, P. H.: Structural properties of diesel exhaust particles measured by transmission electron microscopy (TEM): Relationships to particle mass and mobility, Aerosol Science and Technology, 38, 881–889, 2004.

Rogers, R. R. and Yau, M. K.: A short course in cloud physics, Pergamon Press, Oxford; New York, 1989.